Electronic Supplementary Material (ESI) for Molecular Systems Design & Engineering.

Supporting Information for:
Design principles for the ultimate gas deliverable capacity material: nonporous to porous deformations without volume change

Matthew Witman*[1], Sanliang Ling[2], Vitalie Stavila[1], Pavithra Wijeratne[1], Hiroyasu Furukawa[3,4] and Mark D. Allendorf*[1]

[1]Sandia National Laboratories, Livermore, California 94551, USA
[2]Advanced Materials Research Group, Faculty of Engineering, University of Nottingham, University Park, Nottingham, UK
[3]Department of Chemistry, University of California, Berkeley, CA 94720, USA
[4]Materials Sciences Division, Lawrence Berkeley National Laboratory, Berkeley,CA 94720, USA

S1. Additional model details

S1.1. Effects of the E_F^R parameters on deliverable capacity

The shape of the framework potential, E_F, impacts the adsorption energy landscape and thus the deliverable capacity of the adsorption model. However, significant variation in parameter selection for eq. (5) still leads to improved DC over the static slit pore. For example, a parameter set that produces an asymmetric single well potential still has favorable DC compared to the static slit pore. The parameters for these two variations are shown in Table S1, where θ' minimizes E_F^R and $D_i(\theta', L_{eq} = 2\sigma)$ is the largest free sphere at that tilt angle. In other words, both materials have drastically improved DC over the static slit pore because their nonporous minimum energy states suppress adsorption at low pressures.

	V_{max}	a	b	c	θ'	$D_i(\theta', L_{eq} = 2\sigma)$	DC
Asymmetric single well	10	$\pi/12$	$\pi/12$	100	26.0	3.0	0.73
Asymmetric double well	20	$\pi/6$	$\pi/12$	50	31.1	2.73	0.94

Table S1: For two slit pores with $M = 4$ and $L_{eq} = 2\sigma$, the parameters of E_F^R (V_{max} [=] kJ/mol, a, b, c [=] kJ/mol), the location of the global minimum (θ') in E_F^R, $D_i(\theta', L_{eq})$ [=] Å, and the DC [=] molec./site are given.

The asymmetric single well potential is plotted in Figure S1c, and the asymmetric double well potential is plotted in Figure S1f. The isotherms resulting from these potentials are shown in blue in Figure S1. Notably, the asymmetric single well potential still demonstrates an inflection in the adsorption isotherm and maintains a larger DC than the optimized static slit pore (Figure 4).

S1.2. Cooperative adsorption effects from $M > 1$

The inflections in the isotherms in Figure 4 are dependent on a sufficiently large M. In other words, the porous state must have the capability to adsorb multiple methane molecules per slit pore in order to obtain the enhancement in deliverable capacity afforded by S-shaped isotherms.

---

*mwitman@sandia.gov ; mdallen@sandia.gov

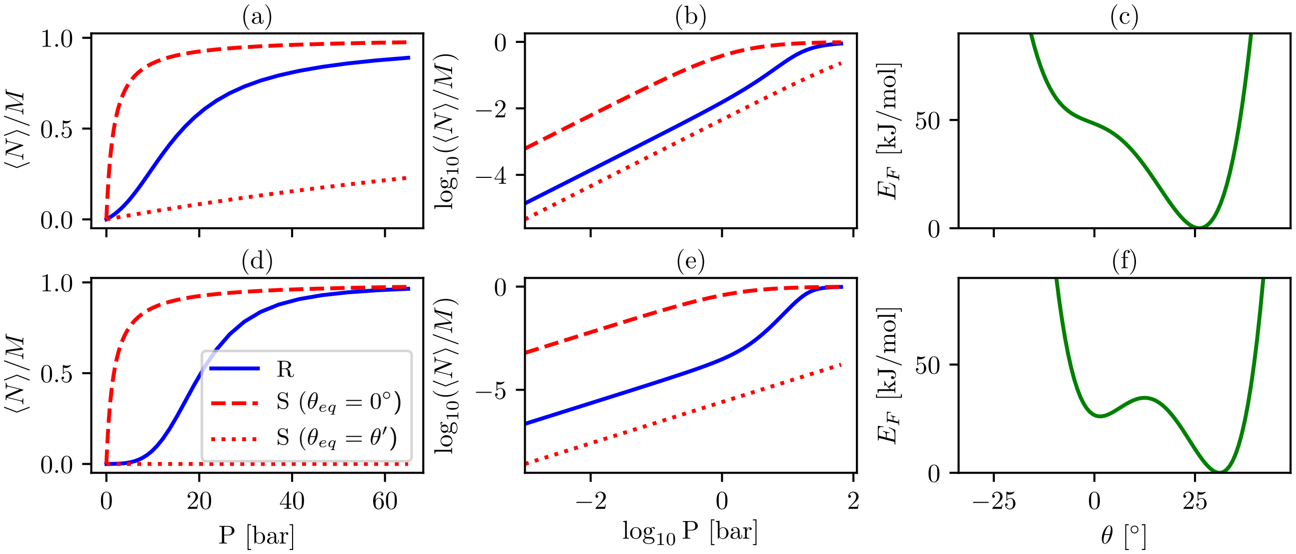

Figure S1: Isotherms plotted on a linear-linear scale (a,d), isotherms repeated on a log-log scale (b,e), and $E_F^R(\theta, L_{eq} = 2\sigma)$ (c,f) for an asymmetric single well potential (a-c) and an asymmetric double well (d-f). Blue isotherms correspond to the he rotating slit pore isotherm, while dashed red lines correspond to the static slit pore with $\theta_{eq} = 0$ and $\theta_{eq} = \theta'$.

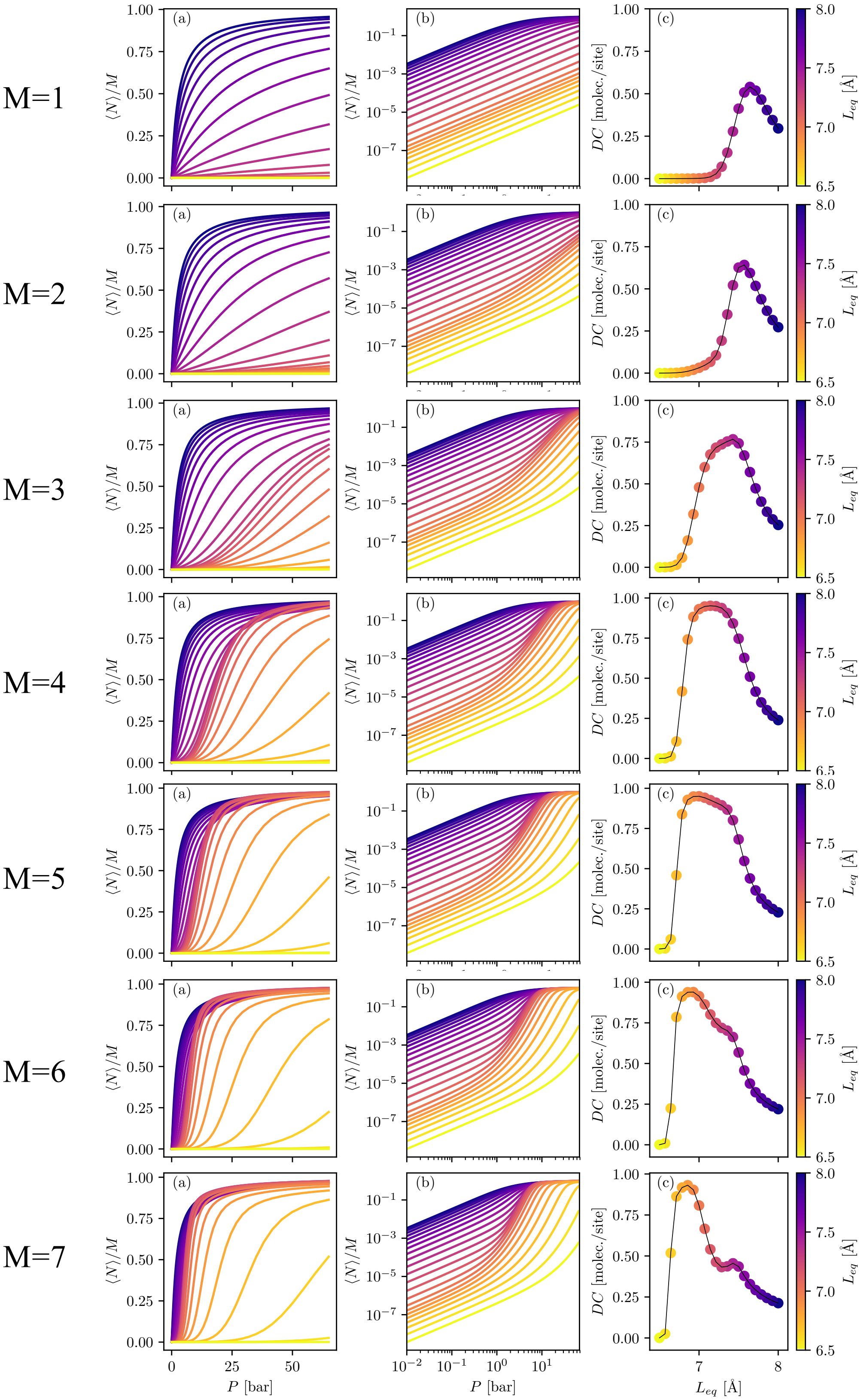

Figure S2: Evolution of the isotherms and deliverable capacity as a function of M and L_{eq}. The first column shows isotherms for various L_{eq}, the second column shows the same data on a log-log scale, and the third column plots the deliverable capacity as a function of L_{eq}.

S1.3. Effect of the spring constant on deliverable capacity in the R+V slit pore

Decreasing the spring constant of the slit pore vibrations in the R+V model continues to shift the optimal L_{eq} of the slit pore to lower values. As k decreases, the reduced L_{eq} is needed to ensure that the nonporous state remains nonporous at low chemical potential despite larger $L > L_{eq}$ fluctuations, but not so low that $\langle L \rangle$ still cannot reach a porous structure at high chemical potential.

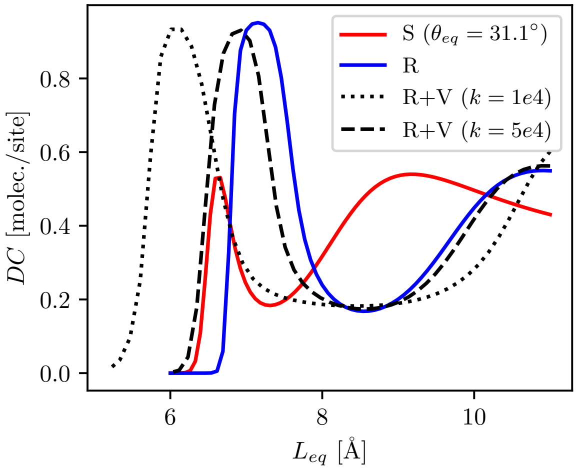

Figure S3: DC vs. L_{eq} for the S, R, and R+V slit pores for the asymmetric double well potential in Table S1, shown for both $k = $ 1e4 and 5e4 J/mol.

S1.4. Adsorption volume discretization

Figure S4 shows $M = 4$ discretization of channel sites within the slit pore. Each channel site has width, $W = 2^{1/6}\sigma_G$, and thus cross-sectional area, $A_{site} = W^2$. We denote the "free area", A_o, as the area in which the particle can translate without overlapping a boundary of an occupied cell. Overlap occurs when the particle's center is less than σ_G from a site boundary. This modeling of particle overlaps is important since such configurations are very high in energy and don't contribute to the partition function. This "free area" in lattice adsorption models is also commonly used to model dead volumes in porous materials.[1] In the case where there are no particles present (visualized by $N = 0$ in Figure S4), $A_o = (2W - \sigma_G)^2/4$. When 2 particles already occupy sites (blacked out cells for the $N = 2$ schematic in Figure S4), $A_o = (2W - \sigma_G)(W - \sigma_G)/2$. For $N = 3$, $A_o = (W - \sigma_G)^2$. These free areas are schematically shown in green in Figure S4.

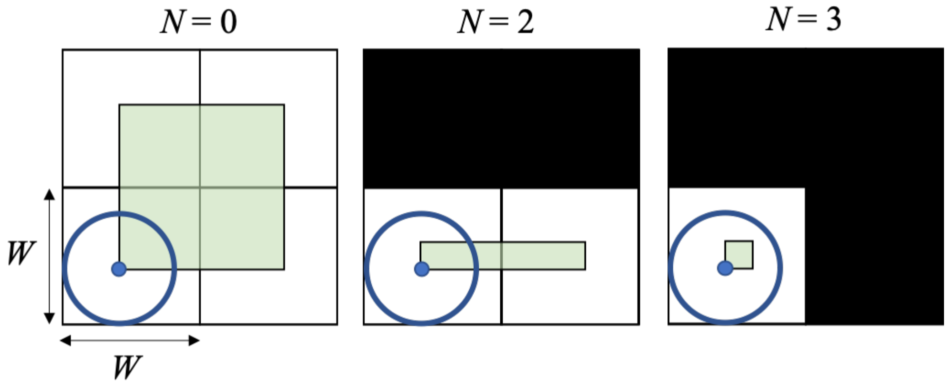

Figure S4: A schematic of the $M = 4$ slit pore model, where each channel site is discretized with cross-sectional area $A_{site} = W^2$. The blue open circle represents the outer diameter of the adsorbate (σ_G), and the filled circle is the adsorbate's center. The free area of each site is schematically shown in green, while cells that are blocked due to the presence of $N = 2$ or $N = 3$ adsorbates are filled in black.

Clearly A_o depends on the number of particles adsorbed in the lattice model, but introduction of this complexity negates our ability to numerically integrate the partition function. Therefore we choose the intermediary A_o value, which yields $A_o = 1.1$ Å^2 when $\sigma_G = 3.73$ Å. In other words, this method of calculating A_o yields the highest fidelity at intermediate loadings, and subsequently overestimates the configurational entropy at high loadings and underestimates it a low loadings. Nonetheless, this discretization is a necessary step to make the model numerically integrable, to account for particle overlaps (i.e. much better than setting $A_o = A_{site}$), and to allow the model results to be mapped to a volumetric basis for comparison with real materials.

S1.5. Code availability

The IPython notebook used to generate all data in this report can be found at: `https://github.com/mwitman1/FlexibleSlitPore.git`

S2. Additional simulation details

S2.1. DFT calculation settings

All density functional theory (DFT) calculations have been performed using the CP2K code, which uses a mixed Gaussian/plane-wave basis set.[2,3] We employed double-ζ polarization quality Gaussian basis sets[4] and a 400 Ry plane-wave cutoff for the auxiliary grid, in conjunction with the Goedecker-Teter-Hutter pseudopotentials.[5,6] All DFT calculations, including single point energies and geometry/cell optimizations, were performed using the PBE functional,[7] with Grimme's D3 van der Waals correction (PBE+D3).[8] This method was shown to give very good agreement with experimental structural data on several MOFs which we studied previously.[9–11] The counterpoise method[12] was used to correct for basis set superposition errors in all binding energy calculations. The initial structures were taken from the experimentally resolved crystal structure of M(NDC) (M = Ca or Sr).[13] Example CP2K input files can be found in the supporting simulation files (S2.4).

S2.2. GCMC simulation details

GCMC simulations were performed using the RASPA code[14] with the TraPPE[15] force field Lennard-Jones parameters for methane and the UFF[16] force field Lennard-Jones parameters for framework atoms. Force field parameter values, structures, and MC sampling settings can be found in the supporting simulation files (S2.4).

S2.3. Isoreticular expansion of Sr(NDC)

More void volume can be imparted to the porous state of Sr(NDC) by performing isoreticular expansion with the hypothetical linkers (HYP, HYP2, HYP3) shown in Figure S5. Each ligand is of equal length (defined as distance between the carboxylic acid groups which form the 1-D SrO rods), but of varying width with $W_{\mathrm{HYP}} < W_{\mathrm{HYP2}} < W_{\mathrm{HYP3}}$. After constructing Sr(NDC) analogs using these hypothetical ligands via a 1-D rod MOF assembly algorithm,[17] we then applied the exact same DFT calculations as were described for Sr(NDC) in the manuscript. Visual comparison of the resulting $\mathrm{F}|_{\mathrm{F}}^{\mathrm{DFT}}$ and $\mathrm{F}|_{\mathrm{F{\cdot}G}}^{\mathrm{DFT}}$ configurations are shown in Figure S6.

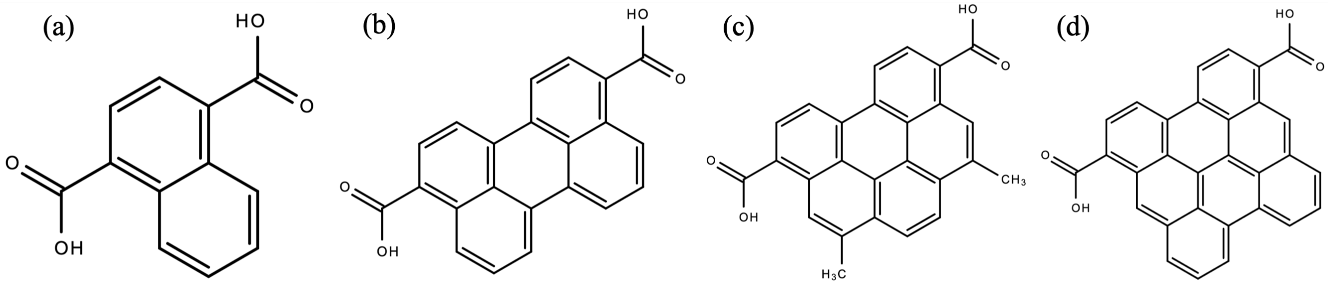

Figure S5: The 1,4-NDC ligand (a) is extended in three hypothetical ligands (b-d) with increasing width.

The geometric differences between the $\mathrm{F}|_{\mathrm{F}}^{\mathrm{DFT}}$ and $\mathrm{F}|_{\mathrm{F{\cdot}G}}^{\mathrm{DFT}}$ configurations between each linker significantly affect the adsorption properties. Again denoting θ' as the linker rotation angle in the $\mathrm{F}|_{\mathrm{F}}^{\mathrm{DFT}}$ state, Figure S6 shows that $\theta'_{\mathrm{HYP}} > \theta'_{\mathrm{HYP2}} > \theta'_{\mathrm{HYP3}}$. This occurs because the wider linkers protrude further into the center of the *bc* face

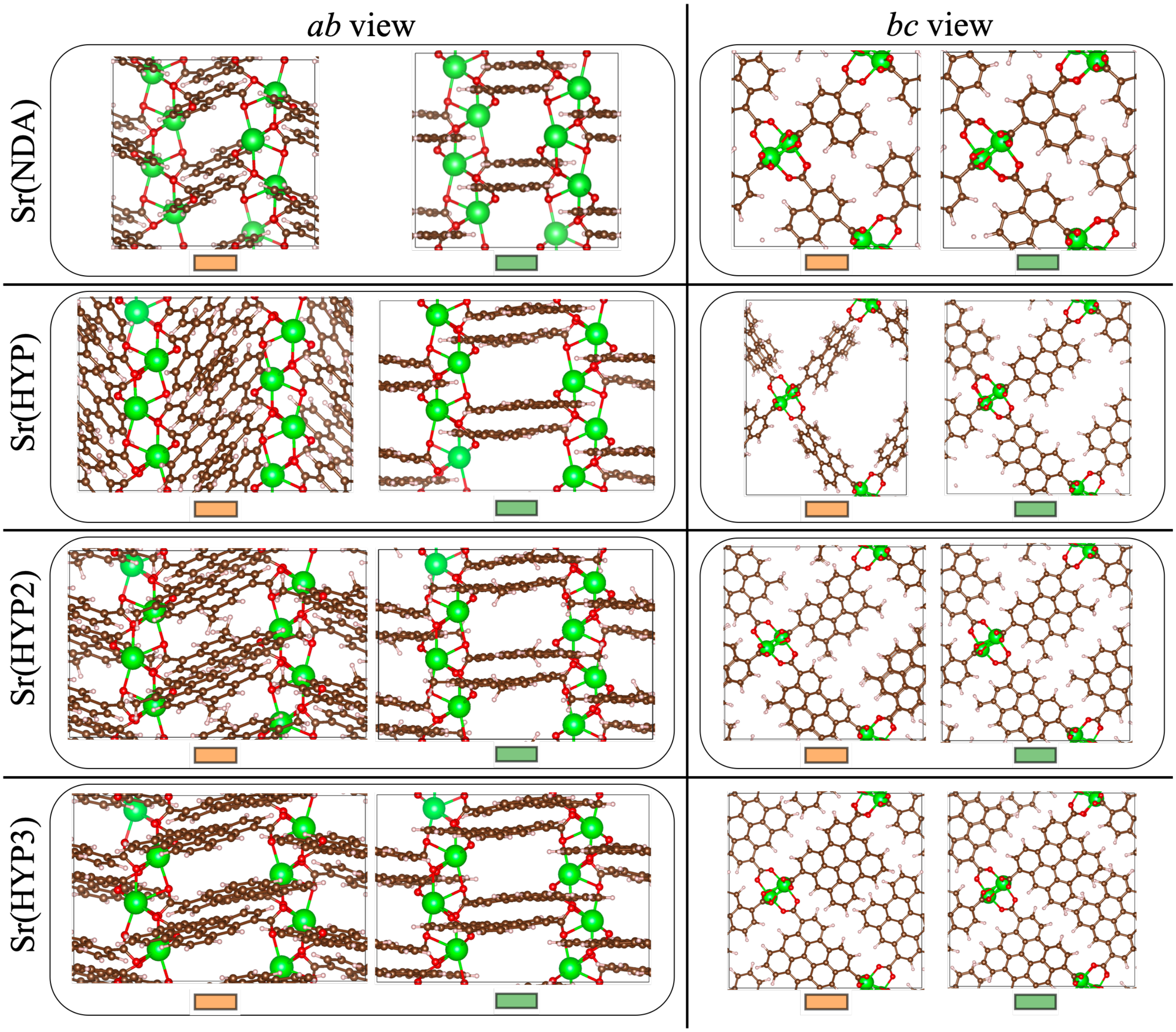

Figure S6: Visualization of the *ab* and *bc* faces of Sr(NDC), Sr(HYP), Sr(HYP2), and Sr(HYP3) structures. The adsorbate-removed, minimum energy configuration ($\mathrm{F}|_{\mathrm{F}}^{\mathrm{DFT}}$) are denoted by the orange patch and methane-added, minimum energy configuration ($\mathrm{F}|_{\mathrm{F\cdot G}}^{\mathrm{DFT}}$) are denoted by the green patch.

(Figure S6), and steric repulsion with the opposite linker reduces how far each can rotate. A higher value of θ' reduces the porosity between the rotating pores, which helps boost *DC*. However, if the linker is not wide enough, a porous channel opens normal to the *bc* face, which also reduces the porosity of the $\mathrm{F}|_{\mathrm{F}}^{\mathrm{DFT}}$ configuration. This is especially noticeable in Sr(HYP). Therefore, a the optimal linker need have the perfect width to prevent adsorption between within the slit pore *and* prevent a channel from existing normal to the *bc* face.

None of the hypothetical linkers, however, achieve the perfect aspect ratio to reproduce the highly nonporous $\mathrm{F}|_{\mathrm{F}}^{\mathrm{DFT}}$ state of Sr(NDC). This can be seen from the adsorption isotherms performed on the $\mathrm{F}|_{\mathrm{F}}^{\mathrm{DFT}}$ state in Figure S7. With HYP, the large porous space in the *bc* face results in significant uptake in $\mathrm{F}|_{\mathrm{F}}^{\mathrm{DFT}}$. HYP2 and HYP3 both show smaller, yet non-negligible uptake due to either too much void space in the middle of the *bc* face or too little linker rotation, respectively. Figure S7 also marks $P = 35$ bar, which is also sometimes selected as the P_{ads} for technical storage targets. Despite the increase in porosity of the $\mathrm{F}|_{\mathrm{F}}^{\mathrm{DFT}}$ configurations, the maximum achievable deliverable capacity of the hypothetical structures with a $P_{ads} = 35$ bar target could be competitive with the record-setting Co(BDP), which exhibits $DC = 155$ v(STP)/v.[18] Taking $\rho|_{35\mathrm{bar}}(\mathrm{F}|_{\mathrm{F\cdot G}}^{\mathrm{DFT}}) - \rho|_{5.8\mathrm{bar}}(\mathrm{F}|_{\mathrm{F}}^{\mathrm{DFT}})$ to be the *maximum possible* deliverable capacity, Table S2 shows how the HYP2 and HYP3 ligands, in the best case scenario, could provide comparable performance to Co(BDP). If a structure could be optimized that, like Sr(NDC), has a more nonporous $\mathrm{F}|_{\mathrm{F}}^{\mathrm{DFT}}$ state, it would then have the potential to exceed Co(BDP) performance with a $P_{ads} = 35$ bar target.

Structure	DC [v(STP)/v]
Sr(NDC)	140
Sr(HYP)	137
Sr(HYP2)	147
Sr(HYP3)	148

Table S2: The maximum possible DC, $\rho|_{35\mathrm{bar}}(\mathrm{F}|_{\mathrm{F{\cdot}G}}^{\mathrm{DFT}}) - \rho|_{5.8\mathrm{bar}}(\mathrm{F}|_{\mathrm{F}}^{\mathrm{DFT}})$, that could be achieved in Sr(NDC), Sr(HYP), Sr(HYP2), or Sr(HYP3) with a $P_{ads} = 35$ bar target.

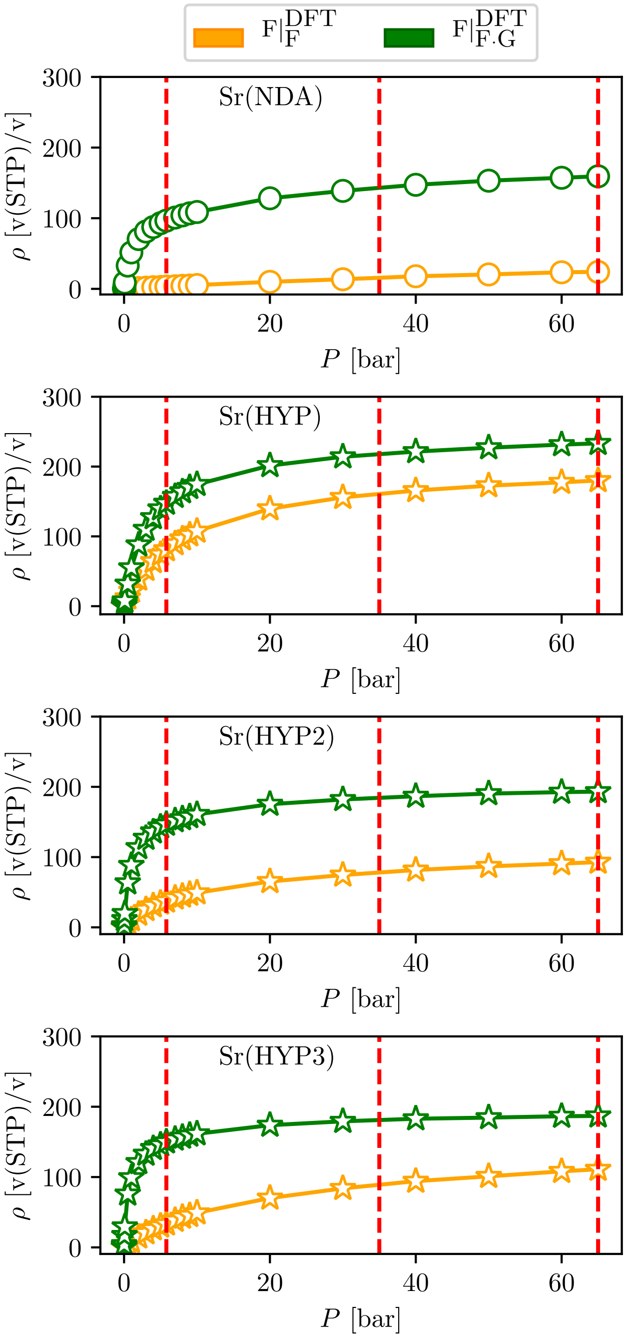

Figure S7: Methane isotherms for Sr(NDC), Sr(HYP), Sr(HYP2), Sr(HYP3) in the adsorbate-removed, minimum energy state (orange = $F|_{F}^{DFT}$) and methane-added, minimum energy configuration (green = $F|_{F \cdot G}^{DFT}$).

S2.4. Supplementary files

The following structural and simulation files are provided in the supplementary_files.zip, as well as the IPython notebook for the slit pore model:

`supplementary_files`
- `FlexSlitPore.ipynb`
- `SrNDC`
  - `KIYMAI-clean_raspa.cif` ($F|_{F}^{DFT}$ configuration)
  - KIYMAI-clean+8CH_4_removed_raspa.cif ($F|_{F \cdot G}^{DFT}$ configuration)
  - `RASPA_files`
    - `simulation.input`

    - force_field_mixing_rules.def
    - psuedo_atoms.def
  - CP2K_files
    - SrNDC.inp (CP2K cell optimization input file for SrNDC)
- Sr_hypothetical_structs
  - SrHYP
    - KIYMAI-Sr-hypo-clean_raspa.cif ($\text{F}|^{\text{DFT}}_{\text{F}}$ configuration)
    - KIYMAI-Sr-hypo-clean+CH_4_removed_raspa.cif ($\text{F}|^{\text{DFT}}_{\text{F}\cdot\text{G}}$ configuration)
  - SrHYP2
    - KIYMAI-Sr-hypo2-clean_raspa.cif ($\text{F}|^{\text{DFT}}_{\text{F}}$ configuration)
    - KIYMAI-Sr-hypo2-clean+CH_4_removed_raspa.cif ($\text{F}|^{\text{DFT}}_{\text{F}\cdot\text{G}}$ configuration)
  - SrHYP3
    - KIYMAI-Sr-hypo3-clean_raspa.cif ($\text{F}|^{\text{DFT}}_{\text{F}}$ configuration)
    - KIYMAI-Sr-hypo3-clean+CH_4_removed_raspa.cif ($\text{F}|^{\text{DFT}}_{\text{F}\cdot\text{G}}$ configuration)
- BilayerGraphene
  - spacing7.500000rot0.000000.cif
  - RASPA_files
    - simulation.input
    - force_field_mixing_rules.def
    - psuedo_atoms.def

S3. Sr(NDC) synthesis and characterization

Sr(NDC) was synthesized via a solvothermal reaction by reacting strontium nitrate with 1,4-naphtalenenaphthalenedicarboxylic acid (1,4-H_2NDA) using a procedure previously described by Raja et al.[13] In order to obtain sufficient powder for hydrogen isotherm measurements, the synthesis was scaled up by a factor of 50 compared to the literature method. This was achieved by conducting the solvothermal synthesis in five 250 mL glass bottles and combining the product. In each 250 mL bottle, 0.43 g of 1,4-H_2NDA was dissolved in 70.0 mL DMF, 20.0 mL EtOH, and 10.0 mL of H_2O. To this solution, 0.85 g of $\text{Sr(NO}_3)_2$ was added and the reaction mixture was stirred at room temperature for 30 min until all the solids completely dissolved. The solution was then placed in an oven at 120 °C for 48 hours. The resulting rod-shaped crystals were washed using 100 mL of EtOH and dried overnight under ambient conditions, then dried in an oven at 80 °C for 2 hours. Total final yield of the dried product was 4.524 g. The activation of Sr(NDC) was conducted prior to hydrogen isotherm measurements by heating the sample for 24 hours at 300 °C in vacuum. The materials were characterized using *in situ* XRD on a Oxford Diffraction Supernova diffractometer in capillary mode using Cu Kα radiation. The samples were loaded into 0.7 mm diameter capillaries inside a glovebox. Measurements were recorded using a CCD detector placed at 77 mm from the samples with an exposure time of 60 seconds. The recorded 2D images were added and integrated to generate a 1D pattern.

References

[1] C. M. Simon, J. Kim, L.-C. Lin, R. L. Martin, M. Haranczyk, and B. Smit, “Optimizing nanoporous materials for gas storage,” *Phys. Chem. Chem. Phys.*, vol. 16, no. 12, p. 5499, 2014.

[2] J. VandeVondele, M. Krack, F. Mohamed, M. Parrinello, T. Chassaing, and J. Hutter, “Quickstep: Fast and accurate density functional calculations using a mixed Gaussian and plane waves approach,” *Comput. Phys. Commun.*, vol. 167, pp. 103–128, apr 2005.

[3] J. Hutter, M. Iannuzzi, F. Schiffmann, and J. VandeVondele, “cp2k: atomistic simulations of condensed matter systems,” *Wiley Interdiscip. Rev. Comput. Mol. Sci.*, vol. 4, pp. 15–25, jan 2014.

[4] J. VandeVondele and J. Hutter, “Gaussian basis sets for accurate calculations on molecular systems in gas and condensed phases,” *J. Chem. Phys.*, vol. 127, p. 114105, sep 2007.

[5] S. Goedecker, M. Teter, and J. Hutter, “Separable dual-space Gaussian pseudopotentials,” *Phys. Rev. B*, vol. 54, pp. 1703–1710, jul 1996.

[6] M. Krack, “Pseudopotentials for H to Kr optimized for gradient-corrected exchange-correlation functionals,” *Theor. Chem. Acc.*, vol. 114, pp. 145–152, sep 2005.

[7] J. P. Perdew, K. Burke, and M. Ernzerhof, “Generalized Gradient Approximation Made Simple,” *Phys. Rev. Lett.*, vol. 77, pp. 3865–3868, oct 1996.

[8] S. Grimme, J. Antony, S. Ehrlich, and H. Krieg, “A consistent and accurate ab initio parametrization of density functional dispersion correction (DFT-D) for the 94 elements H-Pu,” *J. Chem. Phys.*, vol. 132, p. 154104, apr 2010.

[9] L. Liu, Z. Chen, J. Wang, D. Zhang, Y. Zhu, S. Ling, K.-W. Huang, Y. Belmabkhout, K. Adil, Y. Zhang, B. Slater, M. Eddaoudi, and Y. Han, “Imaging defects and their evolution in a metal–organic framework at sub-unit-cell resolution,” *Nature Chemistry*, vol. 11, pp. 622–628, May 2019.

[10] S. Ling and B. Slater, “Dynamic acidity in defective UiO-66,” *Chem. Sci.*, vol. 7, no. 7, pp. 4706–4712, 2016.

[11] C. Nanthamathee, S. Ling, B. Slater, and M. P. Attfield, “Contradistinct Thermoresponsive Behavior of Isostructural MIL-53 Type MetalOrganic Frameworks by Modifying the Framework Inorganic Anion,” *Chem. Mater.*, vol. 27, pp. 85–95, jan 2015.

[12] S. Boys and F. Bernardi, “The calculation of small molecular interactions by the differences of separate total energies. Some procedures with reduced errors,” *Mol. Phys.*, vol. 19, pp. 553–566, oct 1970.

[13] D. S. Raja, J.-H. Luo, C.-T. Yeh, Y.-C. Jiang, K.-F. Hsu, and C.-H. Lin, “Novel alkali and alkaline earth metal coordination polymers based on 1,4-naphthalenedicarboxylic acid: synthesis, structural characterization and properties,” *CrystEngComm*, vol. 16, no. 10, p. 1985, 2014.

[14] D. Dubbeldam, S. Calero, D. E. Ellis, and R. Q. Snurr, “RASPA: molecular simulation software for adsorption and diffusion in flexible nanoporous materials,” *Mol. Simul.*, vol. 42, pp. 81–101, jan 2016.

[15] B. Chen and J. I. Siepmann, “Transferable Potentials for Phase Equilibria. 3. Explicit-Hydrogen Description of Normal Alkanes,” *J. Phys. Chem. B*, vol. 103, pp. 5370–5379, jun 1999.

[16] A. K. Rappe, C. J. Casewit, K. S. Colwell, W. A. Goddard, and W. M. Skiff, “UFF, a full periodic table force field for molecular mechanics and molecular dynamics simulations,” *J. Am. Chem. Soc.*, vol. 114, pp. 10024–10035, dec 1992.

[17] M. Witman, S. Ling, S. Anderson, L. Tong, K. C. Stylianou, B. Slater, B. Smit, and M. Haranczyk, “In silico design and screening of hypothetical MOF-74 analogs and their experimental synthesis,” *Chem. Sci.*, vol. 7, no. 9, pp. 6263–6272, 2016.

[18] J. A. Mason, J. Oktawiec, M. K. Taylor, M. R. Hudson, J. Rodriguez, J. E. Bachman, M. I. Gonzalez, A. Cervellino, A. Guagliardi, C. M. Brown, P. L. Llewellyn, N. Masciocchi, and J. R. Long, “Methane storage in flexible metalorganic frameworks with intrinsic thermal management,” *Nature*, vol. 527, pp. 357–361, nov 2015.